Research Article | Vol. 31, No. 17 / 14 Aug 2023 / *Optics Express* 27106
Optics EXPRESS

Gallium arsenide optical phased array photonic integrated circuit

Michael Nickerson,[1,*] Bowen Song,[1] Jim Brookhyser,[2] Gregory Erwin,[2] Jan Kleinert,[2] and Jonathan Klamkin[1]

[1] *Department of Electrical and Computer Engineering, University of California, Santa Barbara, CA 93106, USA*
[2] *MKS Instruments, Photonics Solutions Division, 14523 SW Millikan Way, Beaverton, OR 97005, USA*
[*] *nickersonm@ece.ucsb.edu*

Abstract: A 16-channel optical phased array is fabricated on a gallium arsenide photonic integrated circuit platform with a low-complexity process. Tested with a 1064 nm external laser, the array demonstrates 0.92° beamwidth, 15.3° grating-lobe-free steering range, and 12 dB sidelobe level. Based on a reverse biased p-i-n structure, component phase modulators are 3 mm long with DC power consumption of less than 5 μW and greater than 770 MHz electro-optical bandwidth. Separately fabricated 4-mm-long phase modulators based on the same structure demonstrate single-sided $V_\pi \cdot L$ modulation efficiency ranging from 0.5 V·cm to 1.22 V·cm when tested at wavelengths from 980 nm to 1360 nm.

1. Introduction

Optical beam steering is increasingly investigated for emerging applications ranging from terrestrial navigation LiDAR [1] to free-space optical communication [2], climate monitoring [3], and even disaster relief [4]. Traditional beam steering methods often utilize rotating sources or gimbals with gross physical movement, resulting in physically large systems that are restricted to Hz-range steering speeds. Optical phased arrays (OPAs) resolve these mechanical limitations by providing electronic beamsteering that avoids moving parts. OPAs are simply optical versions of the familiar RF phased arrays that have been employed since the 1940s [5], forming a single large effective aperture by aligning the phase of multiple subapertures to coherently interfere their output in the far field.

Photonic integrated circuit (PIC) technology provides a scalable platform for OPAs. To date, most integrated OPA research has focused on silicon photonics (SiPh) and operation near 1550 nm [6–11]. Shortcomings of SiPh technology include the use of phase modulators based on thermally-induced effects that are limited to MHz modulation speeds with high power dissipation, or carrier-based phase modulators which are faster but suffer from high residual amplitude modulation (RAM) [12–15]. The silicon bandgap also limits operation to wavelengths greater than 1100 nm, thereby excluding the region near 1000 nm commonly utilized for topographical and remote-sensing LiDAR [16–18]. Additionally, on-chip gain and lasers for SiPh are only possible with complex integration techniques involving flip-chip or wafer bonding. In contrast, group III-V compound semiconductor platforms offer native optical gain, lasers, and efficient low-RAM phase modulation mechanisms.

OPAs based on III-V compound semiconductors have primarily focused on indium phosphide (InP) PIC platforms in the 1300 nm and 1550 nm telecommunications wavelength regions. Low power OPAs have been demonstrated on these platforms, some with on-chip gain [19–25]. However, InP PICs are not suitable for shorter wavelengths and typically have high manufacturing costs.

Gallium arsenide (GaAs), another III-V material, has long been employed to build discrete optical components [26–29]. While the development of PIC technology has been focused on the

#492556 https://doi.org/10.1364/OE.492556
Journal © 2023 Received 6 Apr 2023; revised 2 Jul 2023; accepted 2 Jul 2023; published 31 Jul 2023

Research Article | Vol. 31, No. 17 / 14 Aug 2023 / Optics Express 27107
Optics EXPRESS

InP system due to its support for common telecommunications wavelengths, GaAs fabrication methods have also been matured by the wide use of this material in high power microwave electronics and diode lasers operating near 900 nm.

GaAs is a promising material for low-RAM phase modulators operating at wavelengths near 1000 nm due to its strong linear (Pockels) and quadratic electro-optic effects [30–34]. These allow for deep phase modulation without relying on free carrier effects, enabling efficient low-RAM modulators. Importantly, GaAs offers integrated gain in the 900-1300 nm range, enabling the possibility of fully monolithic OPA PICs [35–37].

In this work, we developed a GaAs PIC platform with low fabrication complexity compared to typical III-V processes, and leveraged it to demonstrate an OPA with 16 channels, illustrated in Fig. 1. The integrated phase modulators exhibited broad bandwidth, high speed, and low RAM. This demonstration does not include on-chip optical gain, but the platform is capable of incorporating gain material without sacrificing OPA performance.

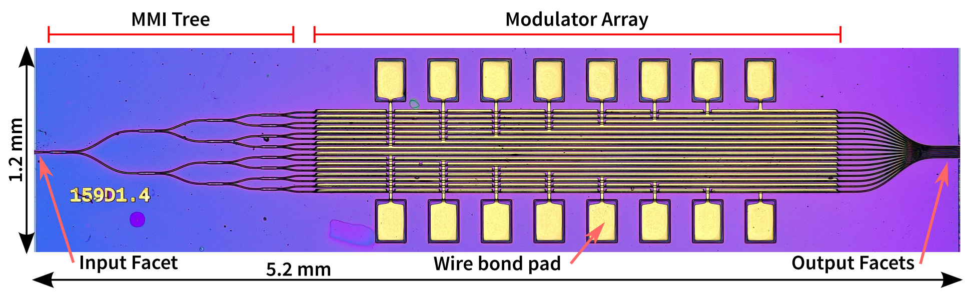

Fig. 1. Optical micrograph of fabricated PIC.

With a single input and an array of phase modulators collapsing to a dense 4-μm-pitch edge-coupled output, this 16-channel PIC OPA achieves a 0.92° beamwidth with 15.3° grating-lobe-free steering range, 12 dB sidelobe level, and greater than 770 MHz single-element electro-optical bandwidth operating at 1064 nm. At 1030 nm, the individual 3-mm-long phase modulators in the OPA demonstrate single-sided $V_\pi \cdot L$ efficiency of 0.7 V·cm, RAM below 0.5 dB for greater than 4π phase modulation [38], and DC power consumption of less than 5 μW at 4π modulation depth. Separately fabricated 4-mm-long phase modulators based on the same structure demonstrate modulation efficiency ranging from 0.5 V·cm to 1.22 V·cm at wavelengths from 980 nm to 1360 nm.

OPA performance was measured with a 1064 nm external laser while the OPA was mounted on and wire bonded to a printed circuit board (PCB), and phase modulation performance was determined using a 1030 nm external laser for both the test structures and mounted PICs as well as a 980 nm external laser and O-band tunable laser for the test PICs. The OPA test wavelength differs from the 1030 nm design wavelength due to equipment limitations at the OPA testing facility.

2. PIC platform design

2.1. PIC architecture

Figure 1 shows a fabricated PIC with a footprint of 5.2 mm × 1.2 mm. The input is a single 4.8-μm-wide deep ridge waveguide with a cleaved facet, designed for higher coupling efficiency from a lensed fiber. The waveguide then tapers to a width of 2 μm and is split into 16 identical channels with a 30-μm pitch via a cascaded tree of 1 × 2 multi-mode interference (MMI) splitters. Each channel comprises identical 3-mm-long, 2-μm-wide, low-power, low-RAM electro-optic phase modulators. The array then collapses to a dense lateral pitch of 4 μm at the output cleaved facet. The PIC was limited to 16 channels to simplify integration and testing, but is readily scalable to significantly higher channel count.

This 16-channel PIC was specifically designed as an OPA demonstrator for this GaAs platform, suitable for a broad range of center wavelengths and continuously usable throughout typical tunable laser ranges. No gain material is present, but the components and epitaxy are engineered for compatibility and simple monolithic integration of conventional GaAs-based quantum wells or quantum dots in the 880-1300 nm range [35–37]. To tailor the design for specific wavelengths of interest, appropriate gain structures would be developed, and slight adjustments to MMI splitter geometry would be made if operating far from the 1030 nm design wavelength used in this work.

2.2. Phase modulators

Careful attention was paid to developing phase modulators ideally suited for OPA applications. Low propagation loss is critical for channel count and output power scaling, and low RAM is necessary for continuous beamforming over the entire steering range. Low power consumption is important for compact portable applications, and high electro-optical bandwidth is required for rapid beam scanning.

To satisfy these requirements, the modulators were designed with a GaAs-based P-p-i-n-N double heterostructure for reverse biased operation, detailed in Table 1. The refractive indices and assumed material losses used for simulation are also listed, and were determined from literature. With a reverse bias applied, this structure yields a high overlap between a nearly linear electric field along the [001] direction and the optical mode, as shown in Fig. 2(a). This high overlap efficiently utilizes the strong linear and quadratic electro-optic effects of GaAs for TE modes propagating in the $[1\bar{1}0]$ direction [30–34]. Additional modulation is available from free carrier effects, but to reduce RAM these are avoided by reverse-biased operation. Figure 2(b) reports the expected phase modulation contributions at 1030 nm for a modulator based on this design. Low optical absorption and RAM are achieved by realizing an 85% overlap between the optical field and the GaAs guiding region, and only a 19% overlap with free carriers at a -10 V bias.

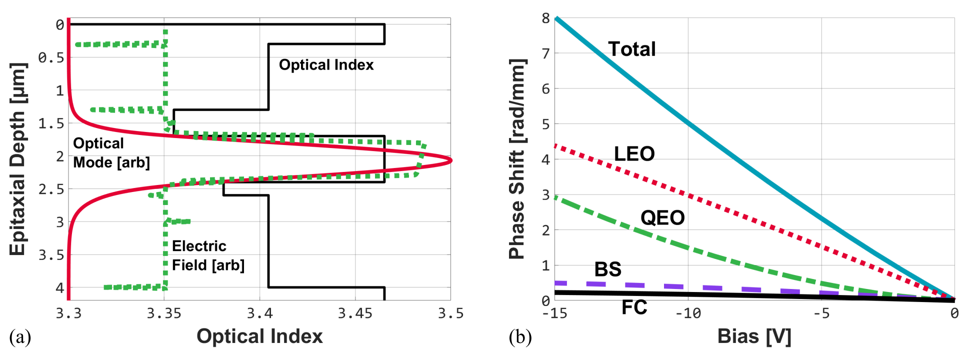

Fig. 2. 1D simulations showing (a) optical index (black), optical mode (red), and electric field (green, dotted), (b) expected phase modulation at 1030 nm (cyan) for this design, including contributions from linear electro-optic (LEO, red, dotted), quadratic electro-optic (QEO, green, dot-dashed), bandgap shift (BS, purple, dashed), and free carrier plasma (FC, black) effects.

The phase modulators were physically implemented as 2-µm-wide deep ridge waveguides with P-contacts deposited on top and an N-contact applied to the backside of the thinned, conductive substrate. A 2.5-µm-thick passivation and isolation material composed of alternating layers of silicon dioxide (SiO_2) and silicon nitride (SiN) is present over the entire PIC. Vias are formed on top of the phase modulator ridges to access the P-contacts, and routing to wire bond pads is

Table 1. Phase modulator epitaxial layer structure

Material	Thickness [nm]	Doping [cm^{-3}]	Refractive Index at 1030 nm	Material Loss at 1030 nm [dB/cm]
GaAs	300	(p) 1e19	3.4653	140
$Al_{0.2}Ga_{0.8}As$	1000	(p) 1e18	3.4046	15
$Al_{0.4}Ga_{0.6}As$	200	(p) 4e17	3.3551	19
$Al_{0.4}Ga_{0.6}As$	200	(p) 2e17	3.3551	11
GaAs	100	(p) 2e17	3.4653	7.2
GaAs	500	UID	3.4653	0.04
GaAs	100	(n) 2e17	3.4653	8.0
$Al_{0.3}Ga_{0.7}As$	200	(n) 2e17	3.3811	13
$Al_{0.2}Ga_{0.8}As$	400	(n) 4e17	3.4046	21
$Al_{0.2}Ga_{0.8}As$	1000	(n) 2e18	3.4046	100
GaAs	300	(n) 3e18	3.4653	120
GaAs	substrate	(n) 1e18	3.4653	40

achieved by metal deposited on top of the isolation material. The P-contacts thus remain present along the entire length of the modulators, and are connected by the top vias to the top routing metal. The routing metal then connects to the appropriate wire bond pads, crossing above other modulators where needed, as shown in the left half of Fig. 3. The cross-modulator routing can also be seen in Fig. 1.

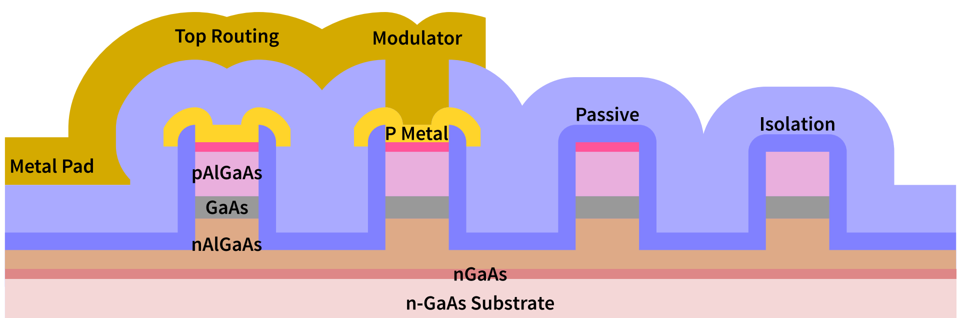

Fig. 3. Cross-section schematic of epitaxy and assorted waveguide structures.

The p-i-n diode is thus formed vertically through the waveguide, with the P-contact on top connected through the top cladding to the p-doped GaAs, the N-contact connected through the substrate and lower cladding to the n-doped GaAs, and the unintentionally doped (UID) middle GaAs layer forming the intrinsic region in the optical guiding layer. When reverse biased, this gives rise to the nearly linear electric field overlapping the optical mode shown in Fig. 2(a).

2.3. Passive components

The remainder of the PIC consists of assorted passive components formed by the single deep ridge etch that is shared with the phase modulators. Passive 2-μm-wide waveguides route the light and have the same structure as the modulators, omitting the metal contacts and top vias. Short segments of waveguides on either end of the modulators are turned into electrical isolation regions by removing the top p-GaAs layer. This prevents the bias applied to the modulator p-contacts from propagating into the surrounding passive waveguide sections and causing undesired phase

Optics EXPRESS

modulation. The right half of Fig. 3 illustrates these passive components, and Fig. 4(a) shows the simulated fundamental TE mode.

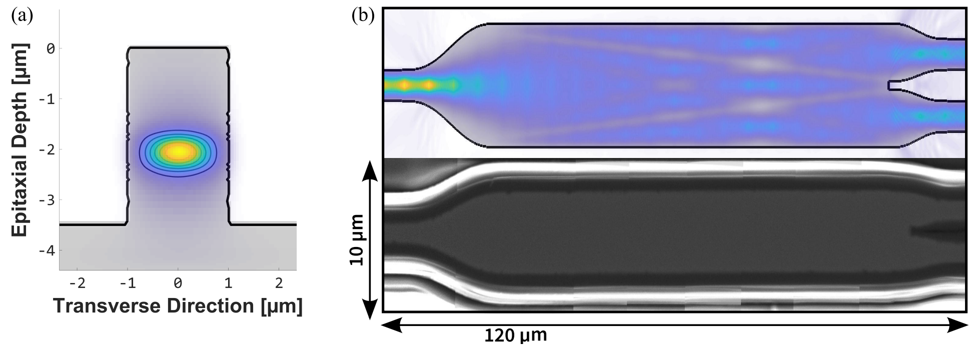

Fig. 4. (a) Simulated fundamental TE optical mode of modulator and passive waveguides (color) and waveguide structure (shaded grey). (b) Simulated (top) and SEM image (bottom, light grey, surrounded by bright and dark dielectric material) of 1 × 2 MMI splitter.

A 2 μm waveguide width was chosen for fabrication simplicity and lithographic resolution constraints, but is not inherently single mode. Single-mode operation is weakly achieved from the stronger bending loss and MMI splitter loss experienced by higher order modes. Strict single-mode operation requires waveguides roughly 0.5 μm wide, which may be fabricated with higher resolution lithography.

Cleaved waveguide facets with antireflection (AR) coating form the single input and 16 outputs. Input light is edge-coupled from a lensed fiber with a 2 μm spot size. As this couples poorly to a 2-μm-wide waveguide, with an expected 5 dB coupling loss, a spot size converter is created by using a 4.8 μm waveguide width at the input facet and tapering it to the nominal 2 μm width over a 60 μm length, resulting in an expected 3 dB coupling loss.

The MMI splitters forming the 1 × 16 splitter share the same passive waveguide structure, with geometry initially determined by standard high contrast MMI ratios [39]. 3D FDTD simulation of the epitaxial structure was performed with commercial tools [40] and used to slightly modify the geometry for optimal performance, as shown in Fig. 4(b).

Center-fed 1 × 2 MMI splitters were selected as an element of the broadband design, and have simulated excess optical loss under 3 dB from 920 nm to 1280 nm. 1 × 4 MMI splitters were also successfully implemented with a 280 μm shorter tree, but are not as broadband (1000-1180 nm); the slight length savings may be traded off against further geometry optimization for specific wavelengths.

3. PIC fabrication

The fabrication process was designed for low fabrication complexity compared to typical III-V and CMOS processes, and consists of seven mask sets, two GaAs etches, and two metal lift-off steps. Figure 5 shows schematic diagrams of the primary fabrication process steps.

The process begins with the deposition of a 400 nm SiO_2 hard mask on clean epitaxy via plasma enhanced chemical vapor deposition (PECVD). Photoresist (PR) is patterned on top of this by an i-line stepper with 0.8 μm effective resolution, defining the waveguide pattern. Unprotected regions of the hard mask are removed by inductively coupled plasma reactive ion etching (ICP-RIE) with CHF_3/CF_4 chemistry, and the waveguides are defined by a 4 μm deep Cl_2/N_2 ICP-RIE etch. Figure 6(a) shows the sidewall of a waveguide immediately after etching. After removing the waveguide hard mask with buffered HF, another hard mask is deposited and patterned, and a $BCl_3/SF_6/N_2$ selective ICP-RIE etch is used to remove the top p + GaAs layer

Optics EXPRESS

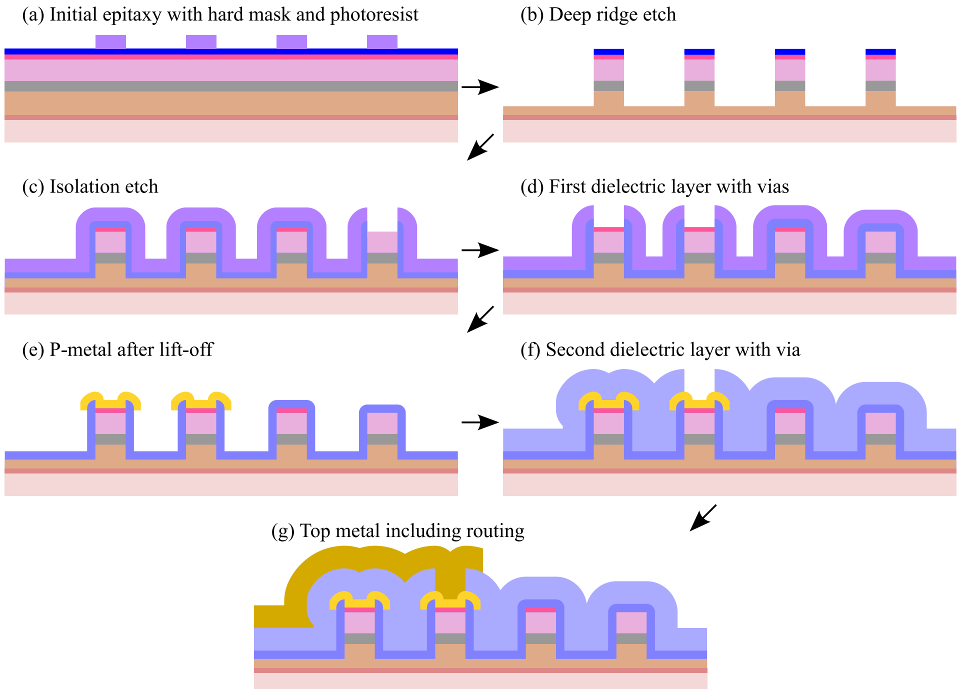

Fig. 5. Schematic diagrams of primary fabrication process steps. (a) Initial epitaxy with hard mask (blue) and patterned photoresist (purple). (b) Deep ridge etch. (c) Isolation etch. (d) First dielectric layer (light blue) with p-via openings. (e) P-metal (yellow) after lift-off. (f) Second dielectric layer (lighter blue) with via opening. (g) Top metal (dark yellow) including routing.

in the electrical isolation regions without etching the top AlGaAs cladding. The isolation-etch hard mask is removed and the devices are passivated with 5 nm Al_2O_3 and 10 nm SiO_2 by atomic layer deposition, on top of which the first dielectric isolation layer of 550 nm total thickness is deposited in alternating SiO_2 and SiN layers via PECVD.

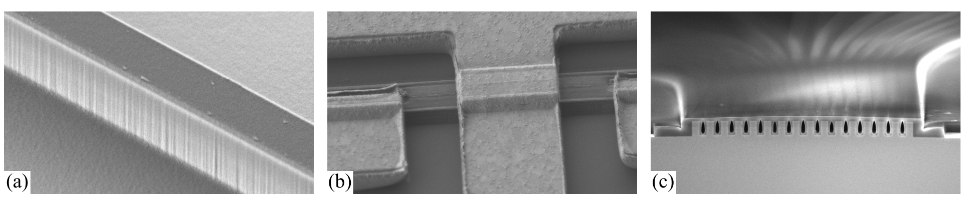

Fig. 6. SEM images of selected fabrication process steps. (a) Deep ridge after first etch. (b) Top metal cross-modulator routing. (c) Output facet after cleaving and AR coating.

The first dielectric isolation layer is selectively opened above the modulator waveguides by a PR mask and CHF_3/CF_4 ICP-RIE etch, and a lift-off mask is defined with negative PR. After depositing 20/40/500 nm of Ti/Pt/Au with electron beam deposition, the metal is lifted off to define the lower metal layer, forming the modulators' top metal contacts. Another PECVD step forms the second dielectric isolation layer with 2 µm total thickness of alternating SiO_2 and SiN layers, and vias are opened to the first metal layer by another ICP-RIE etch on a PR mask. The second lift-off step with 3 µm of Ti/Au then forms the top metal layer for routing and wire bond pads. Shown in Fig. 6(b) is a cross-modulator trace formed by this second lift-off step. A final lithography and ICP-RIE etch defines cleave lanes by removing all dielectric layers from selected areas. To complete fabrication, the substrate is thinned to approximately 200 µm, 10/50/100/20/500 nm of Ni/Ge/Au/Ni/Au N-metal is deposited on the back side, and devices are rapidly thermally annealed in forming gas at 400°C then 480°C for 10 seconds each.

After electrical testing to determine initial yield, selected dies are separated, facets are formed by mechanical cleaving, AR coatings are applied to the facets, and individual PICs are singulated. Figure 6(c) shows a typical cleaved and AR coated output facet, and Fig. 7(a) illustrates the scale of a singulated 16-channel PIC. Individual PICs are then mounted to aluminum nitride carriers with electrical traces and wire bonded. The PIC-on-carriers are then soldered and wire bonded to PCBs as shown in Fig. 7(b).

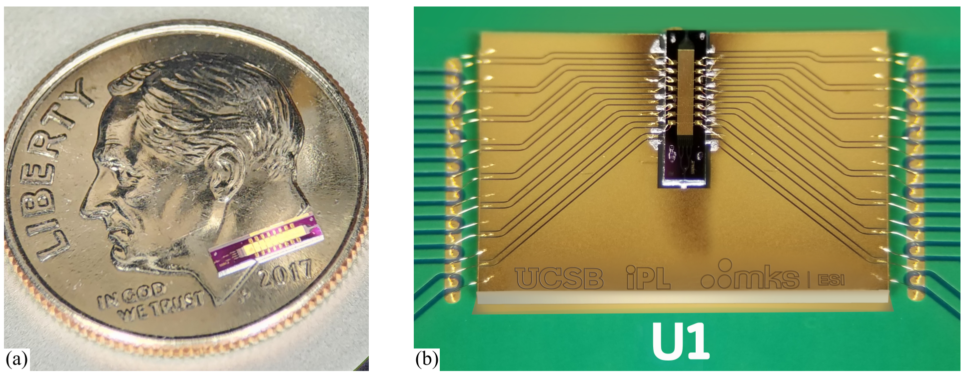

Fig. 7. (a) Photograph of 16-channel PIC on US dime. (b) Photograph of PIC-on-carrier on PCB, retouched for clarity.

4. Characterization

4.1. Phase modulator optical performance

Optical measurement is performed by edge coupling a lensed fiber into the cleaved-facet PIC input, with the PIC mounted on a copper block thermoelectrically cooled to 20°C. Packaged 980 nm and 1030 nm fiber-coupled lasers and an O-band tunable laser provide the light.

Phase modulators are primarily characterized with single-sided Mach-Zehnder modulator (MZM) test PICs comprising a single input, a 1×2 MMI splitter, a 4-mm-long phase modulator on one arm, a 2×1 MMI splitter, and a single output. The electro-optic modulation response is found by rapidly sweeping the bias and recording the simultaneous bias and MZM transmission waveforms on a digital signal oscilloscope, then transforming these to transmission as a function of bias by matching timeseries data. An accurate estimate of the phase modulation $\Delta\phi$ and RAM $\Delta\alpha$ as a function of bias is obtained by simultaneously fitting multiple normalized measurements to the analytical power transmission T of a single-sided unbalanced-loss MZM. The MZM is modeled as an input electric field E_0 that is split into two arms and then coherently recombined, with field E_1 left unmodulated and field E_2 passing through the phase modulator:

$$E_1 = (1-k)\,E_0;\; E_2 = k\,E_0\,e^{i\,\Delta\phi - \Delta\alpha/2} \tag{1}$$

$$\begin{aligned} T &= F\,|E_1 + E_2|^2/E_0^2 + (1-F) \\ &= 1 + F\,k\left(-2 + k + k\,e^{-\Delta\alpha}\right) - 2\,F\,(k-1)\,e^{-\Delta\alpha/2}\cos(\Delta\phi) \end{aligned} \tag{2}$$

where k is the splitting ratio and F is the fraction that is coherently recombinable. Fixed propagation losses and common phase evolution are ignored. To reduce the degrees of freedom,

Optics EXPRESS

the phase modulation and RAM are empirically parameterized by physically motivated but arbitrary fitting functions of the bias potential V, with $V<0$ in reverse biased operation:

$$\Delta\phi(V) = p_1(V_0 - V) + p_2(V_0 - V)^2 \tag{3}$$

$$\Delta\alpha(V) = \mathrm{a}_1\ \exp(a_2(V_1 - V))\ (1 - \tanh[V - V_1])/2 \tag{4}$$

where V_0 = 1.62 V represents the intrinsic electrical field across the p-i-n junction with a value chosen from charge-transport simulations. Parameters k, F, V_1, p_1, p_2, a_1, and a_2 are fit at each measured wavelength. The choice of the $\Delta\phi$ function is motivated by considering the LEO and QEO effects as the primary sources of phase modulation, and the small carrier effects sufficiently characterized by a quadratic fit. The RAM parameterization $\Delta\alpha$ includes a tanh function to behave as constant until some turn-on bias V_1, below which it exponentially increases. The fits are valid only within the limits of measurement, $V \geq$ -12 V and $\Delta\alpha \leq 6$ dB.

Tested at wavelengths from 980 nm to 1360 nm, the 4-mm-long devices in the MZM test PICs demonstrate single-sided V_π·L modulation efficiency ranging from 0.5 V·cm to 1.22 V·cm for the TE optical mode, as shown in Fig. 8(a). RAM is negligible until the onset of Franz-Keldysh electroabsorption, reaching 0.5 dB at a bias of -4.2 V at 980 nm (>3.5π rad), -7.6 V at 1030 nm (~5π rad), and equipment-limited -12 V at 1260 nm (>4.5π rad) and longer.

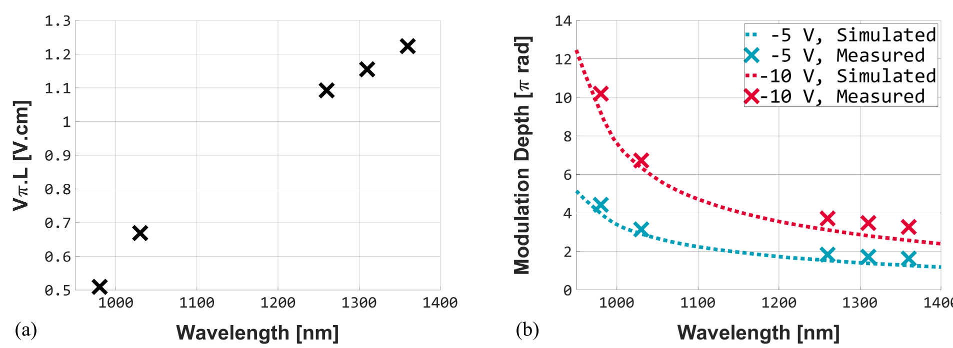

Fig. 8. (a) 4-mm-long phase modulator efficiency at various wavelengths. (b) Simulated (lines) and measured (crosses) phase modulation of 4-mm-long devices at various wavelengths and biases.

These results from the 4-mm-long modulators in MZM structures are also verified at 1030 nm by comparison to measurements of individual 3-mm-long modulators in the 16-channel PICs. This is performed with a self-heterodyne technique in which a selected phase modulator is treated as a single arm of a fiber-optic MZM while the other arm is offset by 150 MHz with an acousto-optic modulator (AOM) [41]. Figure 9 shows a diagram of this arrangement. The laser output is split with a fiber-optic splitter, one output is coupled into the PIC and out of one modulator, and the other output is frequency shifted with a fiber-coupled AOM. After recombining in a fiber-optic splitter, the output of the photodiode is equivalent to a phase-shift-keyed (PSK) signal with a carrier frequency equal to the AOM shift and the phase shift equal to the phase applied by the modulator. The PSK waveform can then be decoded with standard IQ demodulation techniques to extract the relative phase shift. By dithering the applied modulation bias with a small amplitude around a DC offset, precise measurements of the phase modulation's first and second derivative and the first derivative of RAM with respect to bias can be obtained at any AC modulation frequency that is less than half the AOM frequency.

By simulating the electric and optical fields of these modulators with commercial solvers [40] and applying well-known literature values for the various GaAs phase modulation effects [30–33,42], the expected performance of these modulators is calculated. Without adjusting any

Optics EXPRESS

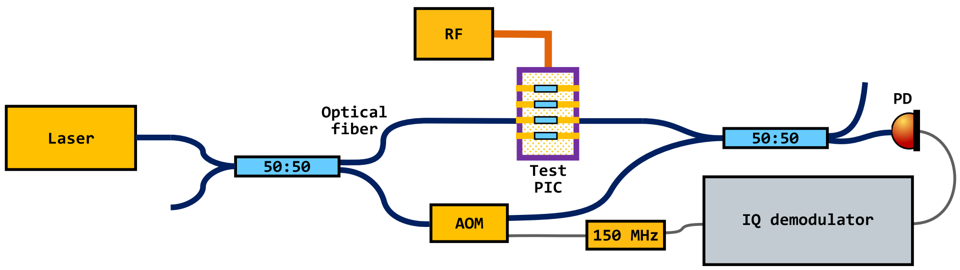

Fig. 9. Diagram of self-heterodyne measurement technique.

model values, the expected performance shown in Fig. 8(b) is in very good agreement with measurements across the full bias and wavelength range. The slight underestimate may be due to free carrier effects, especially at longer wavelengths where the electro-optic effects are weak, as literature coefficients for free carrier effects are inconsistent.

4.2. Phase modulator electrical performance

Detailed input-reflection (S11) electrical measurements are performed with a network analyzer on several PCB-mounted PICs. The expected electrical transmission (S12) and relative contributions of the packaging and PIC are determined by separately characterizing the packaging PCB and applying a lumped-element model to fit the resistance, capacitance, and inductance of the PCB, carrier, PIC, and wire bonds to the S11 measurements. From this, the PIC modulators are determined to have $5 \pm 3\ \Omega$ series resistance and 3.6 ± 0.2 pF capacitance. The expected 3 dB electrical bandwidth of the phase modulators on mounted PICs is 700 MHz, and minor changes to the PCB are identified that should increase this to 1.4 GHz.

Direct electro-optical responsivity is characterized by modulating a single channel and measuring the photodiode response at a selected point in the far-field output, demonstrating a 6 dB bandwidth between 770 MHz and 1 GHz for several channels of a selected PIC, as shown in Fig. 10(a). This agrees with the simulated electrical bandwidth, as power modulation relates to the square of the phase modulation for small signals.

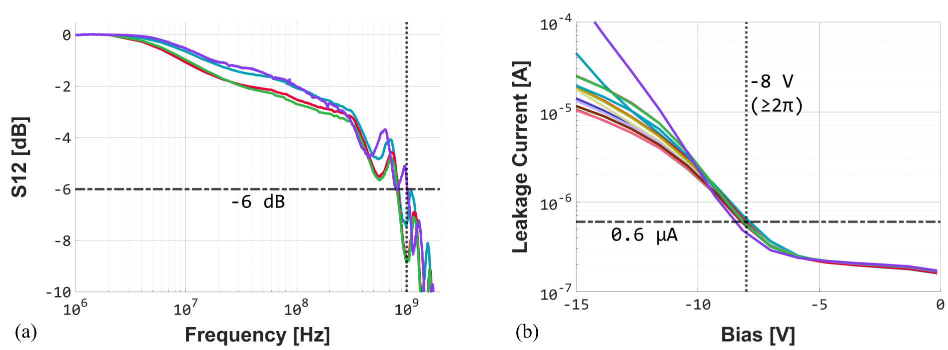

Fig. 10. (a) Electro-optical response of 4 channels of a selected PIC. (b) DC leakage current under reverse bias for all 16 channels of a selected PIC.

The modulation bandwidth of these 3-mm-long phase modulators is ultimately limited by their capacitance, and is thus reducible by shortening the modulators. At 1030 nm, modulators only 1 mm long could provide a full 2π phase shift with 1 dB RAM. GaAs is also amenable to traveling-wave electrode designs exceeding 40 GHz bandwidth [43–45].

DC electrical testing of the 3-mm-long modulators on a selected PIC, plotted in Fig. 10(b), shows leakage currents under 0.6 μA at -8 V bias for all measured modulators, corresponding to less than 5 μW DC power and at least 2π modulation depth at all tested wavelengths. The full 16-channel PIC thus requires under 80 μW to hold any steering angle.

As indicated in Table 2, these optical and electrical metrics are competitive with most InP, SiPh, and lithium niobate on insulator (LNOI) modulators from literature, demonstrating higher speed than SiPh thermal modulators, lower RAM than carrier-injection modulators, and higher $V_{\pi}\cdot L$ modulation efficiency than LNOI modulators at similar wavelengths.

4.3. Optical phased array performance

Key metrics for OPAs are the full-width half-maximum beamwidth – the grating-lobe-free steering range within which the beam can be unambiguously directed without confusion with a grating lobe – and the sidelobe level (SLL) or background level. From the beamwidth and steering range, the number of unique addressable points can be computed, which is a scale-free metric that does not depend on the linear transformations possible with optical lens systems. The number of addressable points is approximately the number of channels for dense linear arrays with ideal beam quality; sparse arrays with nonuniform offsets between channels are able to trade worsened SLL for more addressable points.

Analytically, the steering range can be estimated by $\arcsin(\lambda/d)$ and the beamwidth by that of an aperture equivalent to the OPA width, $\sim\lambda/D$, where λ is the free-space wavelength, d is the distance between emitters, and D is the width of the OPA. The envelope of the steered lobe is determined by the single-emitter beam pattern.

In the case of this PIC tested at $\lambda = 1064$ nm, $d = 4$ μm, and $D = (16-1)\cdot d = 60$ μm, the expected steering range is 15° and expected beamwidth is ~1°, and the number of addressable points is ~15. These results are confirmed by directly propagating the simulated output facet optical mode to the far field [66]; the simulated steering range is 15.2° with a 0.85° beamwidth for ~17 addressable points. The SLL of 13 dB is limited by the sinc^2 function of the far-field pattern of a uniform aperture [67], and cannot be reduced without nonuniform emitter spacings or output powers.

The phased-array performance and output pattern of the selected PIC is evaluated using the experimental setup shown schematically in Fig. 11. The PIC-on-carrier mounted on a PCB is secured to an optical bench, and a lensed fiber on a 3-axis fiber alignment stage couples a 1064 nm laser into the PIC's input facet. An in-line fiber polarizer adjusts the input as needed for optimal polarization. The output of the PIC is captured by a 4 mm effective focal length (EFL) objective lens with a 0.65 numerical aperture, and then a 500 mm EFL relay lens re-images the emitter plane to a 500 μm effective emitter spacing.

Past the reimaged emitter plane, the beam is split with a 3° wedge prism; one surface reflection travels through a pair of relay lenses that reproduce the intermediate focal plane on a monitoring camera. The other surface reflection is propagated to the far field and collimated onto an Ophir LT665 beam profiling camera with a 1147 mm EFL lens, while an identical lens images the transmitted far field beam onto a photodiode. The beam profiling camera may be moved to the near field position for near field data collection.

The output phase of each channel is offset by an unknown amount due to differing path lengths and fabrication imperfections, so the LOCSET algorithm [68] is used to cohere the OPA output by applying the requisite phase modulation to each channel to maximize the signal on the far-field photodiode. To steer the output, the photodiode is moved on a micrometer, and the LOCSET algorithm adjusts emitter phases to shift the peak of the beam to the new location. The positional beam profile is converted to an angular profile at the OPA output by backing out the optical transformations: $\theta_{OPA} = \frac{x_{camera}}{1147\text{ mm}} \cdot \frac{500}{4}$. Data is captured at the 4.54-μm pixel pitch of the beam profilometer, corresponding to 0.028° angular resolution at the OPA output.

Table 2. Phase modulator performance comparison

Year	Platform	Wavelength [nm]	Method[a]	Length [mm]	$V_\pi \cdot L$[b] [V·cm]	RAM @ 2π [dB]	EO Bandwidth
This work	GaAs	980-1360	EO	3, 4	0.5-1.22	<0.5	1 GHz
2020 [46]	GaAs	980	EO	5	1.15	-	20 MHz
2014 [47]	GaAs	780	EO	2	1.5	-	13 MHz
2013 [48]	GaAs	1550	EO	7	0.42	1	-
2008 [49]	GaAs	1550	EO	7	0.3	<1	-
1998 [50]	GaAs	1310	EO	2	0.52	~3	2.5 GHz[c]
1991 [51]	GaAs	1064	EO	1.8	1.9	-	2 GHz[c]
1990 [42]	GaAs	1090	EO	5.3	1.3	~3	-
2021 [52]	InP	1550	carrier	0.8	0.2 mA·cm	-	1 GHz[c]
2013 [24]	InP	1520-1570	carrier	0.2	0.2 mA·cm	1.5	100 MHz
2023 [19]	InP	1550	EO	3.5	1.02	-	-
2022 [21]	InP	1480-1550	EO	2.5	1.2	<0.5	-
2014 [44]	InP	1550	EO	10	1.6	-	67 GHz
2020 [20]	InP	4600	thermal	2.35	53 mW·cm	-	-
2023 [53]	LNOI	784	EO	8	1.6	-	100 GHz
2023 [54]	LNOI	850	EO	5.5	1.56	-	>20 GHz
2023 [54]	LNOI	1550	EO	5.5	2.58	-	>40 GHz
2023 [55]	LNOI	400-700	EO	8	0.34-0.96	-	>20 GHz
2021 [56]	LNOI	1064	EO	7	3.82	-	-
2018 [57]	LNOI	1550	EO	5	4.4	0.1	100 GHz
2019 [58]	LNOI + SiPh	1550	EO	3	4.4	-	70 GHz
2018 [59]	LNOI + SiPh	1550	EO	5	13.4	-	106 GHz
2020 [14]	SiPh	1550	carrier	0.5	0.03	5	324 MHz
2013 [60]	SiPh	1550	EO	0.75	2	3.2	27 GHz
2008 [61]	SiPh	1550	EO	1	6	2.8	30 GHz
2022 [6]	SiPh	1550	thermal	1.5	0.7 mW·cm	-	18 kHz
2020 [62]	SiPh	488	thermal	-	-	-	50 kHz
2020 [63]	SiPh	1560	thermal	0.5	0.8 mW·cm	-	200 kHz
2019 [12]	SiPh	1550	thermal	-	-	2.4	10 kHz
2018 [64]	SiPh	1550	thermal	0.44	1.1 mW·cm	-	-
2014 [9]	SiPh	1480-1580	thermal	-	-	~0	7.3 kHz
2011 [65]	SiPh	1555	thermal	-	-	-	-

[a] "EO" = electro-optic reverse biased, "carrier" = carrier injection, "thermal" = thermo-optic effect
[b] Single-sided; doubled where push-pull is reported.
[c] Not measured, expected RC limit reported.

Figure 12(a) shows the measured beam profile at 0° steering compared to expected performance. Measured beamwidth is 0.92° with 15.3° steering range and 12 dB SLL, differing from simulation by only 8%, 0.7%, and 1 dB respectively. Capturing further beam profiles at additional steering angles, shown in Fig. 12(b), the PIC output reproduces the expected envelope and maintains performance with 0.93° ± 0.01° beamwidth and 12.1 ± 0.4 dB SLL across the entire grating-lobe-free steering range as indicated in Fig. 12(c).

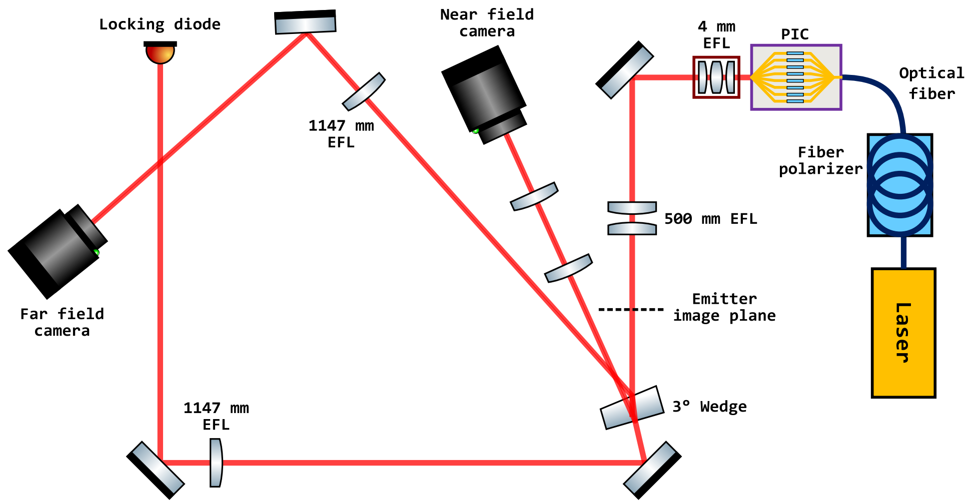

Fig. 11. Schematic of OPA optical measurement setup. Not to scale.

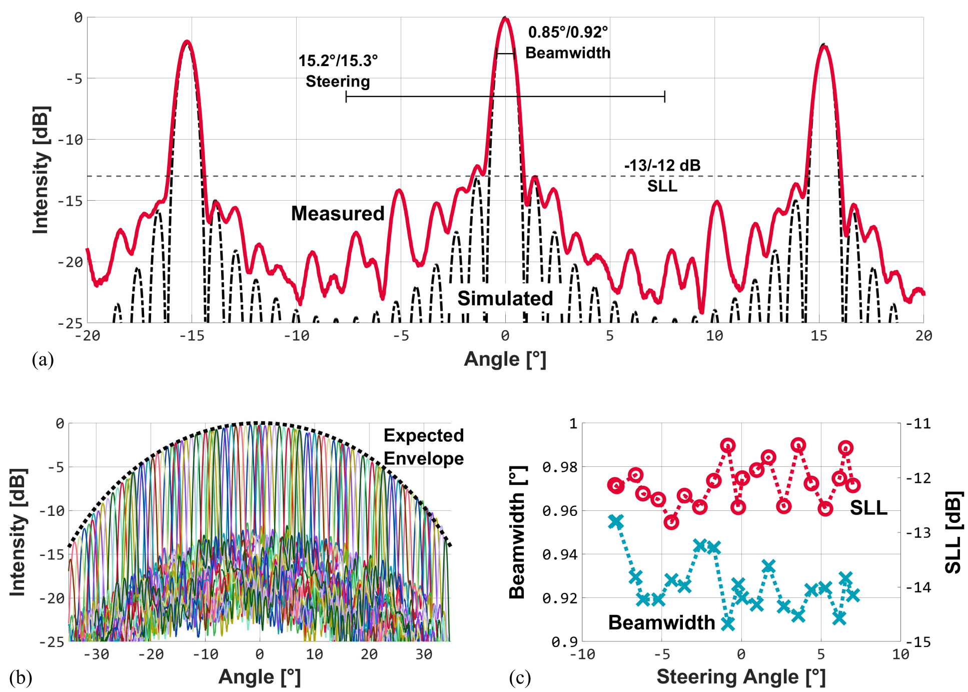

Fig. 12. (a) Simulated (black, dashed) and measured (red, solid) beam profiles with indicated simulated/measured beam width, steering range, and sidelobe level. (b) Measured beam profiles at 21 different steering angles (colored, solid), compared to expected envelope (black, dotted). (c) Beamwidth (left, crosses) and sidelobe level (right, circles) at measured steering angles.

Optics EXPRESS

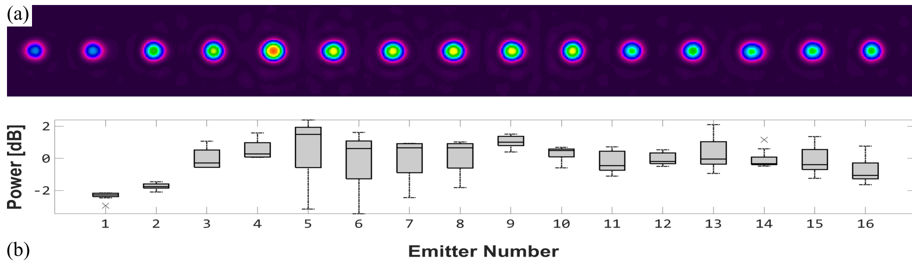

Fig. 13. (a) Typical image of PIC output facets. (b) Distribution of per-channel output power for 12 separate input fiber alignments with median (line), 25th to 75th percentile limits (box), 10th to 90th percentile limits (whiskers), and outliers (crosses).

The slight difference between expected and measured steering range may be due to minor imprecision in the measurement optics, pattern scale errors during fabrication, or a combination of both. Fabrication scale error is expected to be under 1%. The higher beamwidth and inferior SLL can be partially attributed to slightly mismatched subaperture phases, as indicated by the lack of clearly resolvable uniform sidelobes, and nonuniform channel powers.

The near field beam profile at zero bias is also captured. A typical output image, Fig. 13(a), shows that power is not evenly distributed amongst all channels. The uniformity exhibits dependence on input fiber position; comparing the per-channel output power across 12 different input alignments in Fig. 13(b), the mean emitter-to-emitter standard deviation across the array is 1.2 dB, and the mean deviation of a single emitter at different input alignments is 0.76 dB. The variation with input alignment and excess power in the center, taken together, indicates likely multi-mode coupling into the MMI splitter tree.

The performance of this OPA is comparable to or better than most other results in the literature, as summarized in Table 3. The SLL of 12 dB is close to the theoretical 13 dB ultimate performance of a uniform linear array and better than the majority of reported results. Beam quality for a uniform array can be judged by comparing the number of addressable points to the number of channels, and this PIC compares favorably to other uniform arrays. Nonuniform arrays can achieve higher addressable points by sacrificing SLL. This PIC demonstrates operation at 1064 nm, which has not been widely demonstrated for OPAs, and is attractive for expanding the potential applications of OPAs.

Optics EXPRESS

Table 3. Optical phased array performance comparison

Year	Platform	Wavelength [nm]	Channels	Steering Range [°]	Beamwidth [°]	Addressable Points	SLL [dB]
This work	GaAs	980 – 1360[a]	16	15.3	0.92	16	12
2020 [46]	GaAs	980	15	30	4.7	6	8
1991 [51]	GaAs	1064	10	20	2	10	-
2023 [19]	InP	1550	32	35	0.46	76	8.2
2022 [23]	InP	1550	30	17	1.49	11	-
2022 [21]	InP	1480–1550	8	17.8	2.5	7	12.8
2021 [52]	InP	1550	100	8.88	0.11	80	6.3
2020 [20]	InP	4600	32	23	0.6	38	-
2013 [24]	InP	1520-1570	8	1.7	0.2	8	10
2023 [69]	LNOI	1500-1600	16	24	2	12	10
2023 [70]	SiPh	1550	120	25	0.31	80	15.1
2023 [71]	SiPh	1550	16	120	≥6.6[b]	<18[b]	10.9
2022 [8]	SiPh	1550	8192	100	0.01	10000	10
2022 [6]	SiPh	1550	256	45.6	0.154	296	10.8
2020 [63]	SiPh	1560	32	18	0.63	28	10
2020 [62]	SiPh	488	64	50	0.17	294	6.05
2020 [72]	SiPh	1525-1600	512	70	0.15	467	7.5
2020 [14]	SiPh	1550	8×8	8.9×2.2	0.92×0.32	66	8.8
2019 [73]	SiPh	1550	128 (2D)	16×16	0.8×0.8	400	12
2018 [64]	SiPh	1550	1024	22.5	0.03	750	9
2016 [74]	SiPh	1260–1360	128	80	0.14	570	-
2014 [9]	SiPh	1480–1580	16	19.6	1.1	17	10
2014 [75]	SiPh	1550	16	51	3.3	15	-
2011 [65]	SiPh	1555	16	14	1.6	8	10

[a]Results reported for 1064 nm.
[b]Extracted from reported figure.

5. Conclusion

This work has successfully demonstrated a 16-channel GaAs-based OPA with 0.92° beamwidth, 15.3° grating-lobe-free steering range, and 12 dB SLL in close agreement with theoretical results. Individual 4-mm-long phase modulators tested from 980 nm to 1360 nm demonstrate single-sided $V_\pi \cdot L$ modulation efficiency of 1.22 V·cm and better with under 0.5 dB RAM, and 3-mm-long phase modulators in the OPA show less than 5 µW DC electrical power and greater than 770 MHz electro-optical bandwidth when mounted on a carrier and PCB.

Efforts are underway to integrate gain with this epitaxy. Early designs include an on-chip 1030 nm distributed Bragg reflector laser source and semiconductor optical amplifiers near the output for power boosting, forming a high emission power fully monolithic integrated OPA with no external optical components. Future work includes the development of vertical grating couplers for use in two-dimensional tiled outputs [73,76]. Additional research may also investigate alternate wavelength and tunable wavelength designs [77,78], which are ideal on-chip light sources for achieving two-dimensional steering with linear arrays of vertical grating couplers via simultaneous phase and wavelength tuning [9,24].

Optics EXPRESS

Acknowledgments. The authors acknowledge Demis John, Paul Verrinder, and Lei Wang for technical discussion, and funding support from MKS Instruments. A portion of this work was performed in the UCSB Nanofabrication Facility, an open access laboratory.

Disclosures. The authors declare no conflicts of interest.

Data availability. Data underlying the results presented in this paper are not publicly available at this time but may be obtained from the authors upon reasonable request.

References

1. S. Royo and M. Ballesta-Garcia, "An Overview of Lidar Imaging Systems for Autonomous Vehicles," Appl. Sci. **9**(19), 4093 (2019).
2. J. Chang, C. M. Schieler, K. M. Riesing, J. W. Burnside, K. Aquino, and B. S. Robinson, "Body pointing, acquisition and tracking for small satellite laser communication," in *Free-Space Laser Communications XXXI* (International Society for Optics and Photonics, 2019), Vol. 10910, p. 109100P.
3. J. Fridlander, F. Sang, V. Rosborough, F. Gambini, S. T. Šuran-Brunelli, J. R. Chen, K. Numata, M. Stephen, L. A. Coldren, and J. Klamkin, "Dual Laser Indium Phosphide Photonic Integrated Circuit for Integrated Path Differential Absorption Lidar," IEEE J. Sel. Top. Quantum Electron. **28**(1: Semiconductor Lasers), 1–8 (2022).
4. S. Mehta, J. Peach, and A. Weinert, "To Expedite Roadway Identification and Damage Assessment in LiDAR 3D Imagery for Disaster Relief Public Assistance," Infrastructures **7**(3), 39 (2022).
5. Y. Blanchard and P. van Genderen, "A German radar chain, facing the British Chain Home during WW II," in *2014 11th European Radar Conference* (2014), pp. 29–32.
6. Z. Zhang, H. Yu, B. Chen, P. Xia, Z. Zhou, Q. Huang, T. Dai, Y. Wang, and J. Yang, "A Tri-Layer Si3N4-on-Si Optical Phased Array with High Angular Resolution," *IEEE Photonics Technol. Lett.* 1 (2022).
7. Y. Xue, Q. Zhang, Y. Ren, Y. Lei, X. Sun, and L. Zhang, "Two-dimensional single-lobe Si photonic optical phased array with minimal antennas using a non-uniform large spacing array design," Appl. Opt. **61**(24), 7158–7162 (2022).
8. C. V. Poulton, M. J. Byrd, P. Russo, B. Moss, O. Shatrovoy, M. Khandaker, and M. R. Watts, "Coherent LiDAR With an 8,192-Element Optical Phased Array and Driving Laser," IEEE J. Sel. Top. Quantum Electron. **28**(5), 1–8 (2022).
9. D. Kwong, A. Hosseini, J. Covey, Y. Zhang, X. Xu, H. Subbaraman, and R. T. Chen, "On-chip silicon optical phased array for two-dimensional beam steering," Opt. Lett. **39**(4), 941 (2014).
10. H. Hashemi, "Monolithic optical phased arrays in silicon," in *2017 22nd Microoptics Conference (MOC)* (IEEE, 2017), pp. 26–27.
11. Y. Liu and H. Hu, "Silicon optical phased array with a 180-degree field of view for 2D optical beam steering," Optica **9**(8), 903–907 (2022).
12. S. Chung, M. Nakai, and H. Hashemi, "Low-power thermo-optic silicon modulator for large-scale photonic integrated systems," Opt. Express **27**(9), 13430–13459 (2019).
13. J. Mulcahy, F. H. Peters, and X. Dai, "Modulators in Silicon Photonics—Heterogenous Integration & and Beyond," Photonics **9**(1), 40 (2022).
14. H. Zhang, Z. Zhang, J. Lv, C. Peng, and W. Hu, "Fast beam steering enabled by a chip-scale optical phased array with 8×8 elements," Opt. Commun. **461**, 125267 (2020).
15. F. Gao, W. Xie, J. Y. S. Tan, C. P. Leong, C. Li, X. Luo, and G.-Q. Lo, "Comprehensive investigation of thermo-optic phase shifters on a multi-layered SiN-on-SOI platform," J. Lightwave Technol. **41**(10), 3108–3114 (2023).
16. A. W. Yu, M. A. Krainak, D. J. Harding, J. B. Abshire, X. Sun, L. Ramos-Izquierdo, J. Cavanaugh, S. Valett, T. Winkert, M. Plants, C. Kirchner, B. Kamamia, R. Faulkner, P. Dogoda, W. Hasselbrack, and T. Filemyr, "A 16-beam non-scanning swath mapping laser altimeter instrument," in *Solid State Lasers XXII: Technology and Devices* (SPIE, 2013), Vol. 8599, pp. 147–161.
17. H. Zhou, Y. Chen, J. Hyyppä, and S. Li, "An overview of the laser ranging method of space laser altimeter," Infrared Phys. Technol. **86**, 147–158 (2017).
18. J. Guo, X. Fei, P. Ge, Z. Li, Y. Lv, and L. Sheng, "A 1064 nm single-photon lidar for three-dimensional imaging," J. Phys.: Conf. Ser. **1983**(1), 012093 (2021).
19. S. Tan, X. Dai, J. Lou, L. Song, C. Liu, Y. Gu, Q. Chen, C. Jiang, X. Yu, Q. Lu, M. Lu, S. Tong, and W. Guo, "Low-power consumption InP-based optical phase arrays with non-uniformly spaced output waveguides," Opt. Express **31**(2), 3199–3211 (2023).
20. J. Midkiff, K. M. Yoo, J.-D. Shin, H. Dalir, M. Teimourpour, R. T. Chen, and R. T. Chen, "Optical phased array beam steering in the mid-infrared on an InP-based platform," Optica **7**(11), 1544–1547 (2020).
21. M. Gagino, M. B. J. Van Rijn, E. A. J. M. Bente, M. K. Smit, and V. Dolores-Calzadilla, "Broadband operation of an InP optical phased array," IEEE Photonics Technol. Lett. **34**(10), 541–544 (2022).
22. L. Jisan, S. Kyunghyun, and L. Changbum, *et al.*, "Real-time LIDAR imaging by solid-state single chip beam scanner," Electron. Imaging **34**, 1–4 (2022).
23. C.-W. Chow, Y.-C. Chang, S.-I. Kuo, P.-C. Kuo, J.-W. Wang, Y.-H. Jian, Z. Ahmad, P.-H. Fu, J.-W. Shi, D.-W. Huang, T.-Y. Hung, Y.-Z. Lin, C.-H. Yeh, and Y. Liu, "Actively Controllable Beam Steering Optical Wireless Communication (OWC) Using Integrated Optical Phased Array (OPA)," J. Lightwave Technol. **41**(4), 1122–1128 (2022).

24. W. Guo, P. R. A. Binetti, C. Althouse, M. L. Mašanović, H. P. M. M. Ambrosius, L. A. Johansson, and L. A. Coldren, "Two-Dimensional Optical Beam Steering With InP-Based Photonic Integrated Circuits," IEEE J. Sel. Top. Quantum Electron. **19**(4), 6100212 (2013).
25. Y. Guo, Y. Guo, C. Li, H. Zhang, X. Zhou, and L. Zhang, "Integrated Optical Phased Arrays for Beam Forming and Steering," Appl. Sci. **11**(9), 4017 (2021).
26. R. N. Hall, G. E. Fenner, J. D. Kingsley, T. J. Soltys, and R. O. Carlson, "Coherent Light Emission From GaAs Junctions," Phys. Rev. Lett. **9**(9), 366–368 (1962).
27. C. D. Dobson, J. Franks, and F. S. Keeble, "Characteristics of GaAs lasers near room temperature," IEEE J. Quantum Electron. **4**(4), 151–154 (1968).
28. F. E. Goodwin, "A review of operational laser communication systems," Proc. IEEE **58**(10), 1746–1752 (1970).
29. I. Hayashi, "Recent progress in semiconductor lasers — cw GaAs lasers are now ready for new applications," Appl. Phys. **5**(1), 25–36 (1974).
30. J. G. Mendoza-Alvarez, L. A. Coldren, A. Alping, R. H. Yan, T. Hausken, K. Lee, and K. Pedrotti, "Analysis of depletion edge translation lightwave modulators," J. Lightwave Technol. **6**(6), 793–808 (1988).
31. J. Faist and F. K. Reinhart, "Phase modulation in GaAs/AlGaAs double heterostructures. I. Theory," J. Appl. Phys. **67**(11), 6998–7005 (1990).
32. S. S. Lee, R. V. Ramaswamy, and V. S. Sundaram, "Analysis and design of high-speed high-efficiency GaAs-AlGaAs double-heterostructure waveguide phase modulator," IEEE J. Quantum Electron. **27**(3), 726–736 (1991).
33. C. A. Berseth, C. Wuethrich, and F. K. Reinhart, "The electro-optic coefficients of GaAs: Measurements at 1.32 and 1.52 µm and study of their dispersion between 0.9 and 10 µm," J. Appl. Phys. **71**(6), 2821–2825 (1992).
34. S. Adachi, "Dispersion of the linear electro-optic coefficients in GaAs," J. Appl. Phys. **72**(8), 3702–3704 (1992).
35. P. A. Verrinder, L. Wang, J. Fridlander, F. Sang, V. Rosborough, M. Nickerson, G. Yang, M. Stephen, L. Coldren, and J. Klamkin, "Gallium Arsenide Photonic Integrated Circuit Platform for Tunable Laser Applications," IEEE J. Sel. Top. Quantum Electron. **28**(1), 1–9 (2022).
36. L. Wang, H. Zhao, B. Shi, S. Pinna, S. S. Brunelli, F. Sang, B. Song, and J. Klamkin, "High Performance 1.3 µm Aluminum-Free Quantum Dot Lasers Grown by MOCVD," in *2020 Optical Fiber Communications Conference and Exhibition (OFC)* (2020), pp. 1–3.
37. J. J. Coleman, "Strained-layer InGaAs quantum-well heterostructure lasers," IEEE J. Sel. Top. Quantum Electron. **6**(6), 1008–1013 (2000).
38. M. Nickerson, P. Verrinder, L. Wang, B. Song, and J. Klamkin, "Broadband Optical Phase Modulator with Low Residual Amplitude Modulation," in *Optica Advanced Photonics Congress (2022)*, Paper IW4B.4 (Optica Publishing Group, 2022).
39. L. B. Soldano and E. C. M. Pennings, "Optical multi-mode interference devices based on self-imaging: principles and applications," J. Lightwave Technol. **13**(4), 615–627 (1995).
40. "Photonics Simulation Software | Ansys Lumerical," https://www.ansys.com/products/photonics.
41. B. Arar, M. Schiemangk, H. Wenzel, O. Brox, A. Wicht, A. Peters, and G. Tränkle, "Method for in-depth characterization of electro-optic phase modulators," Appl. Opt. **56**(4), 1246–1252 (2017).
42. J. Faist and F. K. Reinhart, "Phase modulation in GaAs/AlGaAs double heterostructures. II. Experiment," J. Appl. Phys. **67**(11), 7006–7012 (1990).
43. R. Spickermann, N. Dagli, and M. G. Peters, "GaAs/AlGaAs electro-optic modulator with bandwidth >40 GHz," Electron. Lett. **31**(11), 915–916 (1995).
44. S. Dogru and N. Dagli, "0.77-V drive voltage electro-optic modulator with bandwidth exceeding 67 GHz," Opt. Lett. **39**(20), 6074–6077 (2014).
45. R. G. Walker and Y. Zhou, "The Design of 50 GHz Gallium Arsenide Electro-Optic Modulator Arrays for Satellite Communications Systems," Front. Phys. **9**, 1 (2021).
46. Z. Wang, J. Liao, Y. Sun, Y. Sun, X. Han, Y. Cao, and R. Zhao, "Chip scale GaAs optical phased arrays for high speed beam steering," Appl. Opt. **59**(27), 8310–8313 (2020).
47. B. Arar, H. Wenzel, R. Güther, O. Brox, A. Maaßdorf, A. Wicht, G. Erbert, M. Weyers, G. Tränkle, H. N. J. Fernando, and A. Peters, "Double-heterostructure ridge-waveguide GaAs/AlGaAs phase modulator for 780 nm lasers," Appl. Phys. B **116**(1), 175–181 (2014).
48. J. H. Shin and N. Dagli, "Ultralow Drive Voltage Substrate Removed GaAs/AlGaAs Electro-Optic Modulators at 1550 nm," IEEE J. Sel. Top. Quantum Electron. **19**(6), 150–157 (2013).
49. J. Shin, Y.-C. Chang, and N. Dagli, "0.3 V drive voltage GaAs/AlGaAs substrate removed Mach–Zehnder intensity modulators," Appl. Phys. Lett. **92**(20), 201103 (2008).
50. Y. T. Byun, K. H. Park, S. H. Kim, S. S. Choi, J. C. Yi, and T. K. Lim, "Efficient single-mode GaAs/AlGaAs W waveguide phase modulator with a low propagation loss," Appl. Opt. **37**(3), 496–501 (1998).
51. D. R. Wight, J. M. Heaton, B. T. Hughes, J. C. H. Birbeck, K. P. Hilton, and D. J. Taylor, "Novel phased array optical scanning device implemented using GaAs/AlGaAs technology," Appl. Phys. Lett. **59**(8), 899–901 (1991).
52. K. Komatsu, Y. Kohno, Y. Nakano, and T. Tanemura, "Large-Scale Monolithic InP-Based Optical Phased Array," IEEE Photonics Technol. Lett. **33**(20), 1123–1126 (2021).
53. F. Valdez, V. Mere, and S. Mookherjea, "100 GHz bandwidth, 1 volt integrated electro-optic Mach–Zehnder modulator at near-IR wavelengths," Optica **10**(5), 578–584 (2023).

Optics EXPRESS

54. Y. Li, T. Lan, D. Yang, J. Bao, M. Xiang, F. Yang, and Z. Wang, "High-Performance Mach–Zehnder Modulator Based on Thin-Film Lithium Niobate with Low Voltage-Length Product," ACS Omega **8**(10), 9644–9651 (2023).
55. S. Xue, Z. Shi, J. Ling, Z. Gao, Q. Hu, K. Zhang, G. Valentine, X. Wu, J. Staffa, U. A. Javid, and Q. Lin, "Full-spectrum visible electro-optic modulator," Optica **10**(1), 125–126 (2023).
56. N. Jagatpal, A. J. Mercante, A. N. R. Ahmed, and D. W. Prather, "Thin Film Lithium Niobate Electro-Optic Modulator for 1064 nm Wavelength," IEEE Photonics Technol. Lett. **33**(5), 271–274 (2021).
57. C. Wang, M. Zhang, X. Chen, M. Bertrand, A. Shams-Ansari, S. Chandrasekhar, P. Winzer, and M. Lončar, "Integrated lithium niobate electro-optic modulators operating at CMOS-compatible voltages," Nature **562**(7725), 101–104 (2018).
58. M. He, M. Xu, Y. Ren, J. Jian, Z. Ruan, Y. Xu, S. Gao, S. Sun, X. Wen, L. Zhou, L. Liu, C. Guo, H. Chen, S. Yu, L. Liu, and X. Cai, "High-performance hybrid silicon and lithium niobate Mach–Zehnder modulators for 100 Gbit s−1 and beyond," Nat. Photonics **13**(5), 359–364 (2019).
59. P. O. Weigel, J. Zhao, K. Fang, H. Al-Rubaye, D. Trotter, D. Hood, J. Mudrick, C. Dallo, A. T. Pomerene, A. L. Starbuck, C. T. DeRose, A. L. Lentine, G. Rebeiz, and S. Mookherjea, "Bonded thin film lithium niobate modulator on a silicon photonics platform exceeding 100 GHz 3-dB electrical modulation bandwidth," Opt. Express **26**(18), 23728–23739 (2018).
60. X. Xiao, H. Xu, X. Li, Z. Li, T. Chu, Y. Yu, and J. Yu, "High-speed, low-loss silicon Mach–Zehnder modulators with doping optimization," Opt. Express **21**(4), 4116–4125 (2013).
61. A. Liu, L. Liao, D. Rubin, J. Basak, Y. Chetrit, H. Nguyen, R. Cohen, N. Izhaky, and M. Paniccia, "Recent development in a high-speed silicon optical modulator based on reverse-biased pn diode in a silicon waveguide," Semicond. Sci. Technol. **23**(6), 064001 (2008).
62. M. C. Shin, A. Mohanty, K. Watson, G. R. Bhatt, C. T. Phare, S. A. Miller, M. Zadka, B. S. Lee, X. Ji, I. Datta, and M. Lipson, "Chip-scale blue light phased array," Opt. Lett. **45**(7), 1934–1937 (2020).
63. W. Ma, S. Tan, K. Wang, W. Guo, Y. Liu, L. Liao, L. Zhou, J. Zhou, X. Li, L. Liang, and W. Li, "Practical two-dimensional beam steering system using an integrated tunable laser and an optical phased array," Appl. Opt. **59**(32), 9985–9994 (2020).
64. S. Chung, H. Abediasl, and H. Hashemi, "A Monolithically Integrated Large-Scale Optical Phased Array in Silicon-on-Insulator CMOS," IEEE J. Solid-State Circuits **53**(1), 275–296 (2018).
65. J. K. Doylend, M. J. R. Heck, J. T. Bovington, J. D. Peters, L. A. Coldren, and J. E. Bowers, "Two-dimensional free-space beam steering with an optical phased array on silicon-on-insulator," Opt. Express **19**(22), 21595–21604 (2011).
66. S. A. Shakir, D. L. Fried, E. A. Pease, T. J. Brennan, and T. M. Dolash, "Efficient matrix approach to optical wave propagation and Linear Canonical Transforms," Opt. Express **23**(20), 26853–26862 (2015).
67. "Phased Array Antenna Patterns—Part 3: Sidelobes and Tapering | Analog Devices," https://www.analog.com/en/analog-dialogue/articles/phased-array-antenna-patterns-part3.html.
68. B. Pulford, "LOCSET phase locking : operation, diagnostics, and applications," Opt. Sci. Eng. ETDs (2012).
69. G. Yue and Y. Li, "Integrated lithium niobate optical phased array for two-dimensional beam steering," (2023).
70. H. Qiu, Y. Liu, X. Meng, X. Guan, Y. Ding, and H. Hu, "Bidirectional high sidelobe suppression silicon optical phased array," Photonics Res. **11**(4), 659–668 (2023).
71. D. Liang, W. Li, X. Wang, X. Zhao, Z. Guo, X. Han, J. Chen, D. Dai, and Y. Shi, "Grating lobe-free silicon optical phased array with periodically bending modulation of dense antennas," Opt. Express **31**(7), 11423–11430 (2023).
72. S. A. Miller, Y.-C. Chang, C. T. Phare, M. C. Shin, M. Zadka, S. P. Roberts, B. Stern, X. Ji, A. Mohanty, O. A. J. Gordillo, U. D. Dave, and M. Lipson, "Large-scale optical phased array using a low-power multi-pass silicon photonic platform," Optica **7**(1), 3–6 (2020).
73. R. Fatemi, A. Khachaturian, and A. Hajimiri, "A Nonuniform Sparse 2-D Large-FOV Optical Phased Array With a Low-Power PWM Drive," IEEE J. Solid-State Circuits **54**(5), 1200–1215 (2019).
74. D. N. Hutchison, J. Sun, J. K. Doylend, R. Kumar, J. Heck, W. Kim, C. T. Phare, A. Feshali, and H. Rong, "High-resolution aliasing-free optical beam steering," Optica **3**(8), 887–890 (2016).
75. A. Yaacobi, J. Sun, M. Moresco, G. Leake, D. Coolbaugh, and M. R. Watts, "Integrated phased array for wide-angle beam steering," Opt. Lett. **39**(15), 4575–4578 (2014).
76. T. Suhara, K. Okada, T. Saso, and H. Nishihara, "Focusing grating coupler in AlGaAs optical waveguide," IEEE Photonics Technol. Lett. **4**(8), 903–905 (1992).
77. P. Verrinder, L. Wang, F. Sang, J. Fridlander, V. Rosborough, M. Nickerson, G. Yang, M. Stephen, L. Coldren, and J. Klamkin, "SGDBR tunable laser on gallium arsenide for 1030 nm lidar applications," in *2021 27th International Semiconductor Laser Conference (ISLC)* (2021), pp. 1–2.
78. P. Verrinder, L. Wang, F. Sang, V. Rosborough, G. Yang, M. Stephen, L. Coldren, and J. Klamkin, "Widely Tunable 1030 nm Gallium Arsenide Sampled Grating Distributed Bragg Reflector Lasers and Photonic Integrated Circuits," in *2022 Optical Fiber Communications Conference and Exhibition (OFC)* (2022), pp. 1–3.